

Laminar-to-Turbulence Transition Modeling for Incompressible Flows in a RANS Framework.

Ginevra Rubino

Postdoctoral Researcher @TUHH (Technical University of Hamburg)

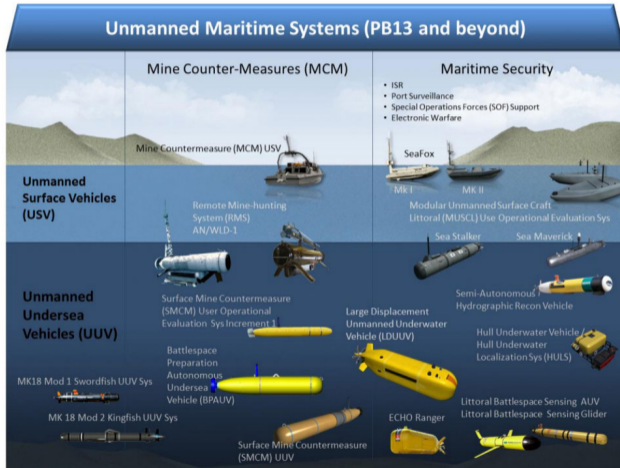
April 30, 2024

- Model scale testing, if tripping not employed;

- Model scale testing, if tripping not employed;
- Methodologies that exploit laminar flow, such as laminar wing design;

- Model scale testing, if tripping not employed;
- Methodologies that exploit laminar flow, such as laminar wing design;
- Wind energy systems, commercial wind turbines (NREL 5 MW, DTU 10 MW, IEA 15 MW) operating in chord-based Re from 3 to 15 millions.

Unmanned Underwater Vehicles



Transition impact:

- Efficiency;
- Maneuvering;
- Power requirements;
- Speed.

Crucial to evaluate the performance of the vehicle with respect to the mission it has been designed for.

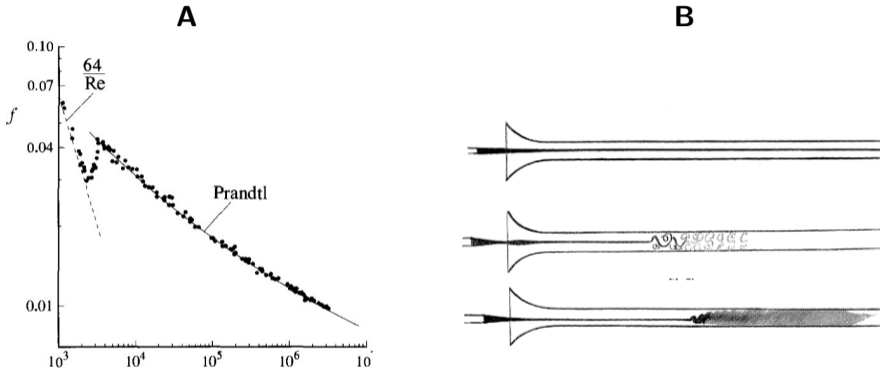
Figure taken from robohub.org.

- 1 Introduction to Transition Mechanisms
- 2 CFD Transition Modeling
- 3 Numerical Results
- 4 Conclusions and Perspectives

Contents

- 1 Introduction to Transition Mechanisms
- 2 CFD Transition Modeling
- 3 Numerical Results
- 4 Conclusions and Perspectives

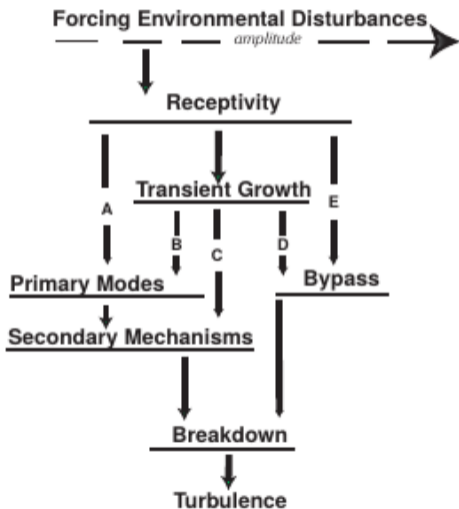
Reynolds Experiments 1883, [1]: Flow in a pipe shows different regimes!



A: Dependence of the friction factor on the Reynolds number for a Poiseuille flow.

B: Sketch of the flow pattern in a pipe using upstream injection of dye for increasing Re .

Basic Transition Onset Mechanism: Transition is not unique!



Receptivity: ambient disturbances (Tu , noise, surface roughness, vibrations...) enter the boundary layer as steady/unsteady fluctuations of the basic state. Establish initial conditions of disturbances amplitude, frequency, phase for the laminar flow breakdown!

- Path A: weak disturbances that grow exponentially.
- Path B/C/D: transient growth (interaction of two non-orthogonal stable modes).
- Path E: very strong disturbances, linear growth is bypassed.

Figure taken from Markovin *et al.*, 1994.

Brief introduction to linear stability¹

Orr-Sommerfeld and Squire Equations: equations for the normal velocity $v' = \tilde{v}(y) \exp(i(\alpha x + \beta z - \omega t))$ and normal vorticity $\eta' = \tilde{\eta}(y) \exp(i(\alpha x + \beta z - \omega t))$

$$\left[(-i\omega + i\alpha U)(D^2 - k^2) - i\alpha D^2 U - \frac{1}{Re}(D^2 - k^2)^2 \right] \tilde{v} = 0,$$

$$\left[(-i\omega + i\alpha U) - \frac{1}{Re}(D^2 - k^2) \right] \tilde{\eta} = -i\beta D U \tilde{v},$$

$\tilde{v} = D\tilde{v} = \tilde{\eta} = 0$ at the wall and in the free-stream.

Setting for the temporal problem, i.e. the spatial structure of the wavelike perturbation rests unchanged, while the wave's amplitude grows or decays in time: $\alpha, \beta \in \mathbb{R}$ are the wave numbers along x and z directions, and $\omega \in \mathbb{C}$ is the frequency.

¹For a complete treatment of this subject please refer to specialized texts as Schlichting, [2], Chandrasekhar, [3], Drazin & Reid, [4], Charru, [5], or Schmid & Henningson, [6].

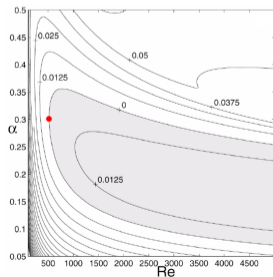
Results from the Orr-Sommerfeld Squire Equations I

- **Squire's theorem:** parallel shear flows become unstable first to 2D perturbations at a lower Re than any Re for which a 3D perturbation exists.

Given $\omega = \alpha c$, c phase speed

$$\left[(U - c)(D^2 - \alpha_{sq}^2) - D^2 U - \frac{1}{i\alpha_{sq} Re_{sq}} (D^2 - \alpha_{sq}^2)^2 \right] \tilde{v} = 0$$

In 2D, for imposed α and Re , $c = c_r + ic_i$ is the eigenvalue of the system $L\tilde{v} = c\tilde{v}$. For $c_i > 0$ disturbances are amplified!



(Re, α) diagram for a Blasius boundary layer flow: contours of constant growth rate c_i . The red dot corresponds to the critical Re and lies on the neutral curve $c_i = 0$.

Figure taken from Schmid [6].

Results from the Orr-Sommerfeld Squire Equations II

- **Rayleigh criterion** for inviscid case: the velocity $U(y)$ has at least an inflection point (free shear layers, jets and wakes):

$$\left[(U - c)(D^2 - \alpha^2) - D^2 U \right] \tilde{v} = 0$$

- For viscous flow, there is an unstable mode **Tollmien-Schlichting** wave, which exists as the viscosity destabilizes the flow for $Re \rightarrow \infty$.

Results from the Orr-Sommerfeld Squire Equations III

- If $\eta \neq 0$, the **Orr-Sommerfeld-Squire system is not-normal**, the operator L does not commute with its adjoint $LL^+ \neq L^+L$. This is the necessary condition for transient growth: an analysis of the eigenvalues cannot capture the dynamics.

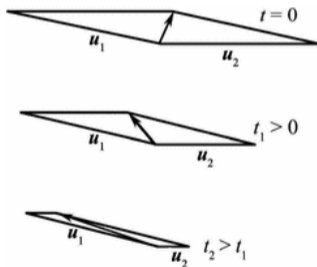


Figure: Sketch illustrating transient growth due to nonorthogonal superposition of two vectors that decay at different rates as time evolves.

Transition Mechanisms

In the following, we distinguish between:

- **Natural Transition:** instabilities arise as exponentially growing eigenmodes;
- **Bypass Transition:** transition that does not emanate from exponential instabilities.

The turbulence intensity Tu is the discriminating factor:

$Tu > 1\%$: Bypass;

$Tu \leq 1\%$: Natural.

Natural Transition

Instability Mechanisms on a Swept Wing

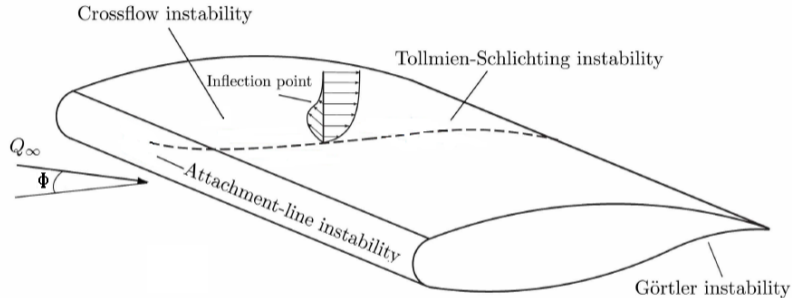


Figure: Different instability mechanisms on the swept wing. Figure reproduced from Shahriari, [7].

Tollmien-Schlichting (T-S) waves.

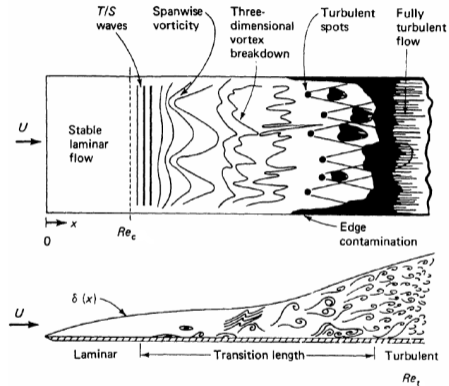


Figure: Schematic representation of the transition process due to T-S waves: streamwise travelling oriented structure of spanwise oriented vorticity, that arise as exponentially growing modes. Figure is reproduced from White & Corfield, [8].

Crossflow Transition

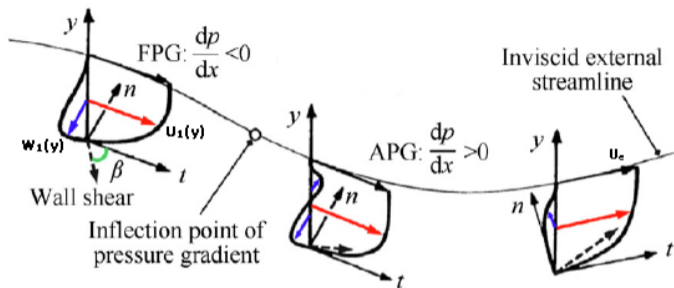


Figure: Development of velocity profiles when suffering from an inflection of the pressure gradient re-adapted from Yiming ,[9]. $U_1(y)$ and $W_1(y)$ are the crossflow and main-flow velocity profiles projected onto a coordinate system relative to the external inviscid streamline.

Leading Edge Contamination

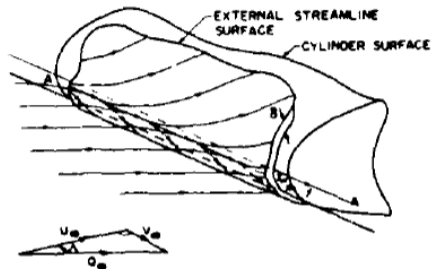


Figure: Schematic representation of the flow near the leading edge of a swept wing, reproduced from Poll, [10]. The linear stability limit calculated by Hall, [11], and confirmed by DNS simulation performed by Spalart, [12], is $\bar{R} = \frac{W_e}{\sqrt{\nu S}} = 583$, i.e. the flow is laminar and stable if $\bar{R} < 583$.

Görtler Vortices on concave surface

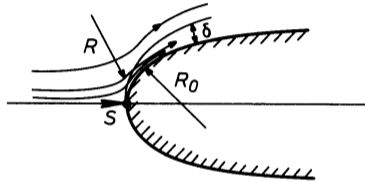


Figure: Görtler vortices at near a stagnation point (S) lying on a concave surface. R is the curvature radius of the external streamline. Figure reproduced from Hirschel *et al.*, [13].

Separation-induced Transition

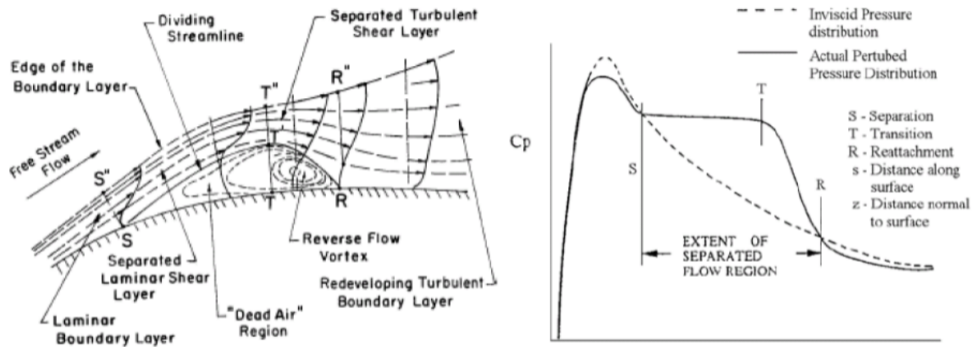


Figure: Schematic representation of a laminar separation bubble: streamlines and velocity profile (left) from O'Meara & Muller, [14] and the experimental pressure coefficient distribution (right) from Lee *et al.*, [15].

Bypass Transition

Bypass Transition .



Figure: Smoke visualization of streamwise streaks appearing in a boundary layer subjected to moderate level of freestream turbulence intensity $Tu = 2.2\%$. The flow, coming from the left, is captured at a certain distance from the leading edge and it transitions (breakdown and turbulence spot formations) in the right edge of the image. Figure reproduced from Matsubara *et al.*, [16].

Contents

- 1 Introduction to Transition Mechanisms
- 2 CFD Transition Modeling**
- 3 Numerical Results
- 4 Conclusions and Perspectives

Modeling Approaches

Modeling Approaches I: DNS and LES

- **DNS** (Direct Numerical Simulations) is the most suitable method to predict transition dynamics, as it solves the full non-linear, time dependent Navier-Stokes equations;
 - Computational time and post-processing prohibitive for targeted Re : total number of grid points $\sim Re^{9/4}$, [17];
 - Specification of the inlet conditions not trivial.
 - Perfect geometry description.
- **LES** (Large Eddy Simulations) is also able to capture transition dynamics, alternative approach to DNS;
 - Griding requirements for wall bounded flows are significant, but less than DNS;
 - Specification of the inlet conditions not trivial, as well as the geometry description;
 - Subgrid-scale model might influence the outcome, wall resolved LES should be preferred, increasing the related computational cost: for a turbulent flow over a flat plate of length L_x , the number of grid points necessary to resolve the Kolmogorov length scale are proportional to Re : WMLES requires $N_{tot} \sim Re$, while WRLES needs $N_{tot} \sim Re^{13/7}$, the estimation for DNS becomes $N_{tot} \sim Re_{L_x}^{37/14}$, [18].

Why moving to RANS?

The main implication with RANS is that the averaging eliminates the linear amplification of the disturbances and the discarded linear effects might seem not compatible with transition physics!

Nevertheless, in many applications, transition occurs in small flow area and it is dictated by geometry features, pressure gradients, and flow separation.

A RANS model is able to capture these effects with sufficient engineering accuracy, upon the inclusion of proper correlations in the models formulation.

Modeling Approaches II: RANS (Reynolds Average Navier Stokes Equations) Framework

- e^N **method** by Smith & Gamberoni, [19] is so far one of the best approaches.
 - Based on linear stability theory and experimental results (critical N_{TS} and N_{CF});
 - Computes the local amplification rate N of a disturbance, i.e. the total growth rate of the most unstable frequency f at transition location, along the streamlines using velocity profiles extracted from boundary-layer code simulations;
 - Not easily integrated within RANS framework;
 - Only provide the transition location;
 - Cannot be used as predictive tool.

Modeling Approaches III: RANS (Reynolds Average Navier Stokes Equations) Framework

- Low- Re RANS models are not calibrated for transition flows and cannot predict transition dynamics;
- RANS turbulence models coupled to local/non-local (systematic stability calculations along streamlines) transition criteria (Abu-Ghannam and Shaw, Arnal-Habillah-Delcourt and its variants, ...).
 - Less adapted to massively parallel computations because of the calculation of boundary layer parameters, θ , H ...
- AFT model (Coder & Maughmer) coupled to Spalart Allmaras model : resolution of a transport equation for the amplification factor \tilde{n} and one for the intermittency γ expressed through its logarithm.

Menter & Langtry Philosophy

- Be formulated locally (no search or line integration operations);

Menter & Langtry Philosophy

- Be formulated locally (no search or line integration operations);
- Allow the inclusion of different transition mechanisms;

Menter & Langtry Philosophy

- Be formulated locally (no search or line integration operations);
- Allow the inclusion of different transition mechanisms;
- Do not affect the underlying turbulence model in fully turbulent regimes;

Menter & Langtry Philosophy

- Be formulated locally (no search or line integration operations);
- Allow the inclusion of different transition mechanisms;
- Do not affect the underlying turbulence model in fully turbulent regimes;
- ? Be formulated independent of the coordinate system (Galilean invariance).

Local Correlation Transition Models (LCTM):

- $\gamma - Re_\theta$ (2009/2012): two transport equations: for the intermittency γ and the transition momentum thickness Reynolds number \bar{Re}_{θ_t} .
- γ (2015): one transport equation for the intermittency γ .

In their original formulation, the models account for 2D natural (T-S waves), bypass and separation induced transition + different criteria for crossflow transition.

Intermittency Equation

$$\frac{\partial(\rho\gamma)}{\partial t} + \frac{\partial(\rho u_j \gamma)}{\partial x_j} = P_\gamma - E_\gamma + \frac{\partial}{\partial x_j} \left[\left(\mu + \frac{\mu_t}{\sigma_\gamma} \right) \frac{\partial \gamma}{\partial x_j} \right]$$

Intermittency Equation

$$\frac{\partial(\rho\gamma)}{\partial t} + \frac{\partial(\rho u_j \gamma)}{\partial x_j} = \boxed{P_\gamma} - E_\gamma + \frac{\partial}{\partial x_j} \left[\left(\mu + \frac{\mu_t}{\sigma_\gamma} \right) \frac{\partial \gamma}{\partial x_j} \right]$$

Intermittency Equation

$$\frac{\partial(\rho\gamma)}{\partial t} + \frac{\partial(\rho u_j \gamma)}{\partial x_j} = \boxed{P_\gamma} - E_\gamma + \frac{\partial}{\partial x_j} \left[\left(\mu + \frac{\mu_t}{\sigma_\gamma} \right) \frac{\partial \gamma}{\partial x_j} \right]$$

	$\gamma - Re_\theta$	γ
P_γ	$c_{a1} F_{\text{length}} \rho S (\gamma F_{\text{onset},2D})^{c_{\gamma 3}} (1 - \gamma)$	$[F_{\text{length}} (\rho S (1 - \gamma) \gamma)] F_{\text{onset},2D}$

Intermittency Equation

$$\frac{\partial(\rho\gamma)}{\partial t} + \frac{\partial(\rho u_j \gamma)}{\partial x_j} = \boxed{P_\gamma} - E_\gamma + \frac{\partial}{\partial x_j} \left[\left(\mu + \frac{\mu_t}{\sigma_\gamma} \right) \frac{\partial \gamma}{\partial x_j} \right]$$

	$\gamma - Re_\theta$	γ
P_γ	$c_{a1} \boxed{F_{\text{length}}} \rho S (\gamma F_{\text{onset},2D})^{c_{\gamma 3}} (1 - \gamma)$	$\boxed{F_{\text{length}}} (\rho S (1 - \gamma) \gamma) F_{\text{onset},2D}$
F_{length}	$f_1(\bar{Re}_{\theta_t})$	100

f_1 is an empirical correlation.

Intermittency Equation

$$\frac{\partial(\rho\gamma)}{\partial t} + \frac{\partial(\rho u_j \gamma)}{\partial x_j} = \boxed{P_\gamma} - E_\gamma + \frac{\partial}{\partial x_j} \left[\left(\mu + \frac{\mu_t}{\sigma_\gamma} \right) \frac{\partial \gamma}{\partial x_j} \right]$$

	$\gamma - Re_\theta$	γ
P_γ	$2F_{\text{length}}\rho S(\gamma \boxed{F_{\text{onset},2D}})^{c_\gamma} (1 - \gamma)$	$[F_{\text{length}}(\rho S(1 - \gamma)\gamma)] \boxed{F_{\text{onset},2D}}$
F_{length}	$f_1(\bar{Re}_{\theta_t})$	100
$F_{\text{onset},2D}$	$\frac{Re_v}{2.193 Re_{\theta_c}}$	$\frac{Re_v}{2.2 Re_{\theta_c}}$

f_1 is an empirical correlation.

The vorticity Reynolds number is defined as $Re_v = \frac{\rho y^2}{\mu} \left| \frac{\partial u}{\partial y} \right| = \frac{y^2 S}{\nu} \sim \frac{\tau_{inertial}}{\tau_{visc}}$.

Intermittency Equation

$$\frac{\partial(\rho\gamma)}{\partial t} + \frac{\partial(\rho u_j \gamma)}{\partial x_j} = \boxed{P_\gamma} - E_\gamma + \frac{\partial}{\partial x_j} \left[\left(\mu + \frac{\mu_t}{\sigma_\gamma} \right) \frac{\partial \gamma}{\partial x_j} \right]$$

	$\gamma - Re_\theta$	γ
P_γ	$c_{a1} F_{\text{length}} \rho S (\gamma F_{\text{onset}})^{c_{\gamma 3}} (1 - \gamma)$	$[F_{\text{length}} (\rho S (1 - \gamma) \gamma)] F_{\text{onset}, 2D}$
F_{length}	$f_1(\bar{Re}_{\theta_t})$	100
$F_{\text{onset}, 2D}$	$\frac{Re_v}{2.193 \boxed{Re_{\theta_c}}}$	$\frac{Re_v}{2.2 \boxed{Re_{\theta_c}}}$

f_1 is an empirical correlation. The vorticity Reynolds number is defined as

$$Re_v = \frac{\rho y^2}{\mu} \left| \frac{\partial u}{\partial y} \right| = \frac{y^2 S}{\nu} \sim \frac{\tau_{inertial}}{\tau_{visc}}$$

Critical Transition Momentum Thickness Reynolds Number Re_{θ_c} Computation

$\gamma - Re_{\theta}$: from the empirical Re_{θ_t} equation to Re_{θ_c} .

$$Re_{\theta_t} = f(Tu, \lambda_{\theta}) \text{ with } \lambda_{\theta} = \frac{\rho \theta^2}{\mu} \frac{dU}{dS} \text{ and } Tu = \sqrt{\frac{2k}{3}} / U.$$

$$\frac{\partial(\rho \bar{Re}_{\theta_t})}{\partial t} + \frac{\partial(\rho u_j \bar{Re}_{\theta_t})}{\partial x_j} = \underbrace{c_{\theta_t} \frac{\rho}{t} (Re_{\theta_t} - \bar{Re}_{\theta_t})(1 - F_{\theta_t})}_{P_{\theta_t}} + \frac{\partial}{\partial x_j} \left[\sigma_{\theta_t} (\mu + \mu_t) \frac{\partial \bar{Re}_{\theta_t}}{\partial x_j} \right].$$

$$Re_{\theta_c} = f_2(\bar{Re}_{\theta_t}) \text{ with } f_2 \text{ empirical correlation.}$$

γ : Re_{θ_c} local empirical correlation.

$$Re_{\theta_c}(Tu_L, \lambda_{\theta,L}) = C_{TU1} + C_{TU2} * e^{-C_{TU3} Tu_L F_{PG}(\lambda_{\theta,L})},$$

where

$$Tu_L = \min \left(100 \frac{\sqrt{2k/3}}{\omega y}, 100 \right) \text{ and } \lambda_{\theta,L} = -7.57 \cdot 10^{-3} \frac{dv}{dy} \frac{y^2}{\nu} + 0.0128.$$

$\gamma - Re_\theta$: from the empirical Re_{θ_t} equation to Re_{θ_c} .

$$Re_{\theta_t} = f(Tu, \lambda_\theta) \text{ with } \lambda_\theta = \frac{\rho\theta^2}{\mu} \left[\frac{dU}{dS} \right] \text{ and } Tu = \sqrt{\frac{2k}{3}} / \left[U \right].$$

$$\frac{\partial(\rho\bar{Re}_{\theta_t})}{\partial t} + \frac{\partial(\rho u_j \bar{Re}_{\theta_t})}{\partial x_j} = \underbrace{c_{\theta_t} \frac{\rho}{t} (Re_{\theta_t} - \bar{Re}_{\theta_t})(1 - F_{\theta_t})}_{P_{\theta_t}} + \frac{\partial}{\partial x_j} \left[\sigma_{\theta_t} (\mu + \mu_t) \frac{\partial \bar{Re}_{\theta_t}}{\partial x_j} \right].$$

$$Re_{\theta_c} = f_2(\bar{Re}_{\theta_t}) \text{ with } f_2 \text{ empirical function.}$$

γ : Re_{θ_c} local empirical formulation.

$$Re_{\theta_c}(Tu_L, \lambda_{\theta,L}) = C_{TU1} + C_{TU2} * e^{-C_{TU3} Tu_L F_{PG}(\lambda_{\theta,L})},$$

where

$$Tu_L = \min \left(100 \frac{\sqrt{2k/3}}{\omega y}, 100 \right) \text{ and } \lambda_{\theta,L} = -7.57 \cdot 10^{-3} \left[\frac{dv}{dy} \right] \frac{y^2}{\nu} + 0.0128.$$

Coupling with $k - \omega$ SST (2003) Turbulence Model

The new transport equation for the turbulence kinetic energy k reads as

$$\frac{\partial(\rho k)}{\partial t} + \frac{\partial(\rho u_j k)}{\partial x_j} = PROD_k - DEST_k + \frac{\partial}{\partial x_j} \left[\left(\mu + \sigma_k \mu_t \right) \frac{\partial k}{\partial x_j} \right],$$

Given P_k and D_k the original turbulence production and destruction, we have:

	$\gamma - Re_\theta$	γ
Production $PROD_k$	$\gamma_{eff} P_k$	$\gamma P_k + P_k^{lim}$
Destruction $DEST_k$	$\min(\max(\gamma_{eff}, 0.1), 1) \cdot D_k$	$\max(\gamma, 0.1) \cdot D_k$

Consideration on the Onset Function

The transition onset criterion based on the vorticity Reynolds number is physically valid only in the laminar flow. The flow is kept transitioning through additional functions: i.e. in γ

$$F_{\text{onset},1} = \frac{Re_V}{2.2Re_{\theta_c}},$$

$$F_{\text{onset},2} = \min(F_{\text{onset},1}, 2.0),$$

$$F_{\text{onset},3} = \max\left(1 - \left(\frac{R_T}{3.5}\right)^3, 0\right),$$

$$F_{\text{onset},2D} = \max(F_{\text{onset},2} - F_{\text{onset},3}, 0).$$

Crossflow Inclusion

Helicity Criterion

The helicity Reynolds number is defined as:

$$Re_{He} = \frac{\rho z^2}{\mu} \frac{He}{U}, \quad He = \mathbf{u} \cdot (\nabla \times \mathbf{u}), \quad U = \sqrt{u^2 + v^2 + w^2}.$$

$$\frac{Re_{He, \max}}{Re_{He_t}} = 1$$

Re_{He_t} is function of the shape factor H_{12} , expressed through the pressure gradient parameter λ_θ , numerically computed (ONERA D, NLF (2)-0415, 6:1 prolate spheroid).

Arnal C1 Criterion (1984)

Crossflow transition due to stationary waves occurs when the following criterion is met:

$$\frac{Re_{\delta_2}}{150f(H_{12})} \geq 1, \quad (1)$$

where

$$f(H_{12}) = \begin{cases} 1 & \text{for } H_{12} \leq 2.3 \\ \frac{2}{\pi} \arctan \left(\frac{0.106}{(H_{12}-2.3)^{2.052}} \right) & \text{for } 2.3 < H_{12} \leq 2.7 \end{cases} \quad (2)$$

Re_{δ_2} is the crossflow Reynolds number and it is defined as

$$Re_{\delta_2} = \frac{U_{1,e}\delta_2}{\nu}, \text{ with } \delta_2 = \int_0^{\infty} \frac{W_1}{U_{e,1}} dy.$$

Based on experimental results around a cylinder, NACA64₂ A 015 profiles, ONERA D profile **at low** Tu .

Local Reconstruction of the C1 criterion

$Tc1$ Reconstruction proposed by Menter.

$$C1 = \frac{Re_{\delta_2}}{150f(H_{12})} \sim \underbrace{F(H_{12})XRe_{stream}}_{non-local} \rightarrow \underbrace{G\Psi Re_{V_{max}}}_{local} = Tc1.$$

- G accounts for the influence of the pressure gradient:

$$G \sim \frac{1}{f(H_{12})} = F(H_{12}).$$

- the indicator Ψ is a non-dimensional measure of the local crossflow strength with respect to the streamwise strength. It is defined as:

$$\frac{Re_{\delta_2}}{Re_{V_{max}}} = X \sim \Psi = \left| \vec{n} \cdot \nabla \left(\frac{\vec{\omega}}{|\vec{\omega}|} \right) \right| y,$$

- $Re_{V_{max}}$ is the local vorticity Reynolds number.

Calibration of the Tc1 using Falkner-Skan-Cooke (FSC) Profiles

The Falkner-Skan-Cooke equations for a 3D laminar boundary layer on an infinite swept wing, i.e. zero spanwise derivative are the key to define a link between local and non-local quantities.

$$f''' + ff'' + \beta(1 - f'^2) = 0$$

$$g'' + fg' = 0$$

$$f, f', g \rightarrow 0 \text{ for } \eta \rightarrow 0; f', g \rightarrow 1 \text{ for } \eta \rightarrow \infty.$$

The solutions f' and g can be combined into the dimensionless streamwise and crosswise velocity components:

$$U_1/U_{1e} = f' \cos(\phi)^2 + g \sin(\phi)^2,$$

$$W_1/U_{1e} = (g - f') \cos(\phi) \sin(\phi).$$

The local functions are reconstructed via the FSC velocity profiles and evaluated at the wall normal position where ΨRe_V has a max.

Calibration of the Tc1 using Falkner-Skan-Cooke (FSC) Profiles

The Falkner-Skan-Cooke equations for a 3D laminar boundary layer on an infinite swept wing, i.e. zero spanwise derivative are the key to define a link between local and non-local quantities.

- Does Ψ well reproduce $XF(H_{12})$?

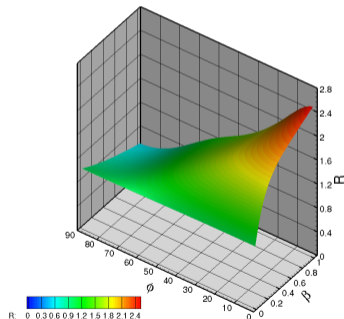
- We define the indicator ratio

$$R(\beta, \phi) = \Psi / (XF(H_{12})),$$

where

$$\left. \begin{array}{l} 0 < \beta \leq 1 \text{ Hartree parameter} \\ 0^\circ < \phi < 90^\circ \text{ Sweep angle} \end{array} \right\} \text{Not known locally.}$$

We want $R \rightarrow 1$



First possible approach

- ϕ is not considered, because not local! β is accounted for through $\lambda_{\theta,CF}$, function of $\frac{dv}{dy} \frac{y^2}{\nu}$.

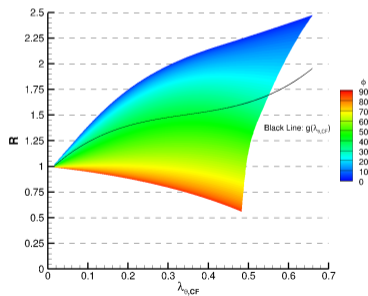
First possible approach

- ϕ is not considered, because not local! β is accounted for through $\lambda_{\theta,CF}$, function of $\frac{dv}{dy} \frac{y^2}{\nu}$.
- Construction of the correction function $G(\lambda_{\theta,CF})$ as a one-variable polynomial of 3rd order.

First possible approach

- ϕ is not considered, because not local! β is accounted for through $\lambda_{\theta,CF}$, function of $\frac{dV}{dy} \frac{y^2}{\nu}$.
- Construction of the correction function $G(\lambda_{\theta,CF})$ as a one-variable polynomial of 3rd order.

$$R = 0.684\Psi/(XF(H_{12}))$$

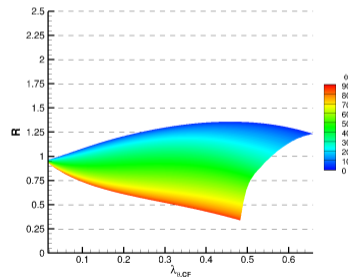
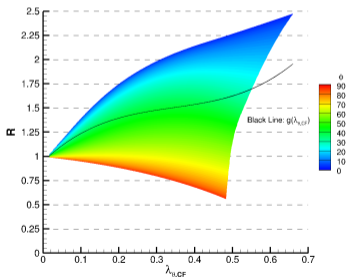


First possible approach

- ϕ is not considered, because not local! β is accounted for through $\lambda_{\theta,CF}$, function of $\frac{dV}{dy} \frac{y^2}{\nu}$.
- Construction of the correction function $G(\lambda_{\theta,CF})$ as a one-variable polynomial of 3rd order.

$$R = 0.684\Psi/(XF(H_{12}))$$

$$R = (G(\lambda_{\theta,CF})\Psi)/(XF(H_{12}))$$

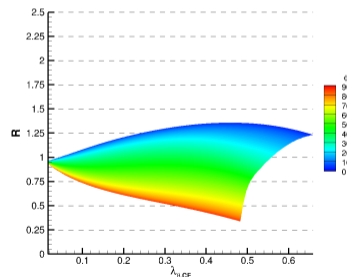
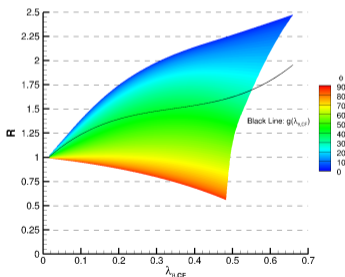


First possible approach

- ϕ is not considered, because not local! β is accounted for through $\lambda_{\theta,CF}$, function of $\frac{dv}{dy} \frac{y^2}{\nu}$.
- Construction of the correction function $G(\lambda_{\theta,CF})$ as a one-variable polynomial of 3rd order.

$$R = 0.684\Psi/(XF(H_{12}))$$

$$R = (G(\lambda_{\theta,CF})\Psi)/(XF(H_{12}))$$



Not accounting for high sweep angles!

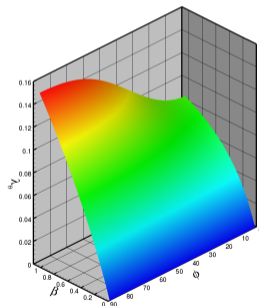
New Calibration I

- ϕ is accounted for in the calibration!

New Calibration I

- ϕ is accounted for in the calibration!
- λ_θ is approximates as a two parameter function (least square method fit):

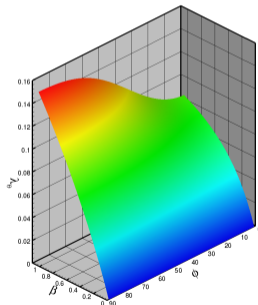
$$\lambda_\theta \sim \lambda_{CF} \left(\frac{dv}{dy} \frac{y^2}{\nu}, \phi \right)$$



New Calibration I

- ϕ is accounted for in the calibration!
- λ_θ is approximates as a two parameter function (least square method fit):

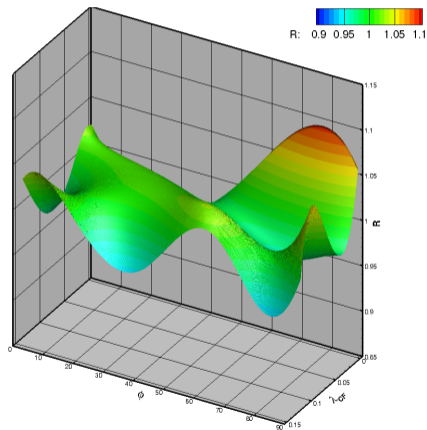
$$\lambda_\theta \sim \lambda_{CF} \left(\frac{dv}{dy} \frac{y^2}{\nu}, \phi \right)$$



- A non-linear polynomial $G(\lambda_{CF}, \phi)$ is used for the correction of the ratio R .

New Calibration II

New corrected ratio $R = (G(\lambda_{CF}, \phi)\Psi)/(XF(H_{12}))$



Maximum deviation from the targeted value is less than 10%

Local sweep angle ϕ calculation

ϕ in FSC is the angle between the external potential flow direction and the local wing attached reference system.

Not CFD-compatible!

$$\phi_L^2 = \arccos \left(\frac{\vec{u}_{wt} \cdot \overline{(\nabla p)_{wt}}}{\|\vec{u}_{wt}\| \|\overline{(\nabla p)_{wt}}\|} \right), \quad \phi_L = \min[\phi_L, \pi - \phi_L].$$

Thus,

$$\cos(\phi_L) = \frac{(\frac{\partial p}{\partial x}, 0, 0) \cdot (u, 0, w)}{\|(\frac{\partial p}{\partial x}, 0, 0)\| \|(u, 0, w)\|} = \frac{u}{\sqrt{(u^2 + w^2)}},$$

At the edge of the b.l.

$$\cos(\phi_L)_e = \frac{u_e}{\sqrt{(u_e^2 + w_e^2)}}.$$

²Defined following Högberg & Henningson, [20].

Inclusion of the criteria in the models formulations

	$\gamma - Re_{\theta}$	γ
$F_{\text{onset}1,CF}$	$\frac{Re_{He}}{C Re_{He,t}^+}$	$\frac{(G(\lambda_{CF}, \phi_L) \psi Re_V)}{C \cdot 150}$

$$F_{\text{onset}2,CF} = \min[\max(F_{\text{onset}1,CF}, 0), 2]$$

$$F_{\text{onset}3,CF} = \max(1 - (R_T/a)^3, 0)$$

$$F_{\text{onset},CF} = \max(F_{\text{onset}2,CF} - F_{\text{onset}3,CF}, 0)$$

a, C are constants calibrated numerically and vary for the two models.

F_{onset} Formulation

The F_{onset} in the P_{γ} is given by the sum $F_{\text{length}} F_{\text{onset},2D} + F_{\text{length},CF} F_{\text{onset},CF}$.

$$F_{\text{length},CF} = 5.$$

Limitation of the criteria

- The crossflow criteria are not Galilean invariant. A strategy might be to use the relative velocity

$$\vec{u}_{rel} = \vec{u} - \vec{u}_{wall}$$

to partially restore Galilean invariance in the boundary layer.

Limitation of the criteria

- The crossflow criteria are not Galilean invariant. A strategy might be to use the relative velocity

$$\vec{u}_{rel} = \vec{u} - \vec{u}_{wall}$$

to partially restore Galilean invariance in the boundary layer.

- Receptivity is neglected, wall roughness is important to account for! Stationary crossflow are excited by small roughness elements.

Contents

- 1 Introduction to Transition Mechanisms
- 2 CFD Transition Modeling
- 3 Numerical Results**
- 4 Conclusions and Perspectives

2D Test Cases chosen within the AVT-313 group

Geometry	α	Re	$Tu_{in}(\%)$	Transition Mechanism	$\nu_{t_{in}}/\nu$
Flat Plate-T3A-		10^7	1.00135	Natural/Bypass	25
Flat Plate-T3A		10^7	5.36609	Bypass	280
NACA0015	5°	1.8×10^5	0.5	Separation-Induced	0.0018
Eppler 387	1° 7°	3×10^5	1	Separation-Induced Natural	0.003

Setting the inlet conditions

$k - \omega$ SST equations for a steady uniform flow, aligned with x^* , reduce to:

$$\frac{dk^*}{dx^*} = -\beta^* k^* \omega^*, \quad \frac{d\omega^*}{dx^*} = -\beta(\omega^*)^2$$

and give the solution for $Tu = \sqrt{(2k/3)}/U$:

$$Tu = \left(Tu_{in} \left(1 + \frac{3(x^* - x_{in})\beta Tu_{in}^2 U^* Re}{2(\nu_{t_{in}}^*/\nu)} \right)^{-\frac{\beta^*}{\beta}} \right)^{0.5}, \quad \text{with } \beta = 0.0828 \text{ and } \beta^* = 0.09.$$

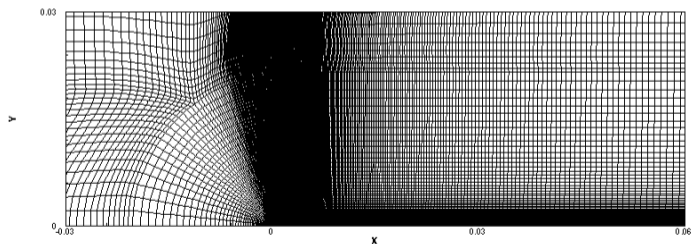
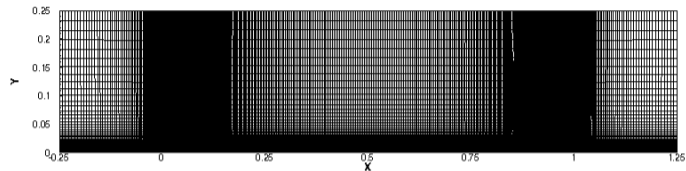
Flat Plate: T3A

Computational Domain

Grid	N_{cells}	$N_{\text{cells-plate}}$	y_{max}^+
1	675840	2048	0.1
2	517440	1792	0.12
3	380160	1536	0.15
4	264000	1280	0.18
5	168960	1024	0.22

Meshes provided by IST Lisbon.

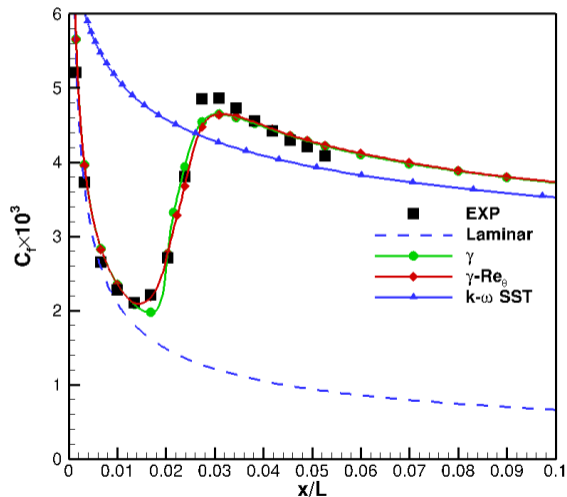
O-Grids were preferred to H-Grids because of the fastest convergence. On an H-grid the highly stretched and high aspect ratio cells downstream of the plate slow down iterative convergence.



T3A Results- Experimental Results from ERCOFTAC

Initial Test Conditions:

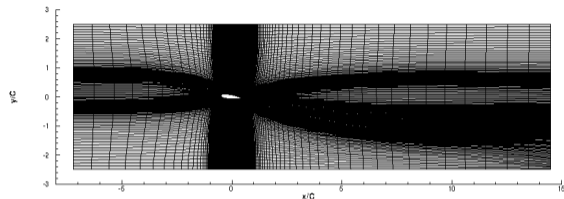
	Re	$Tu_{in}(\%)$	$\nu_{t_{in}}/\nu$	$Tu(\%)$
			270	2.23
T3A	10^7	5.36609	280	2.465
			290	2.502



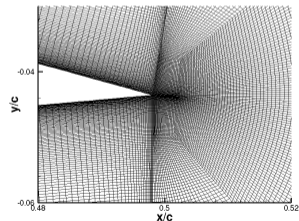
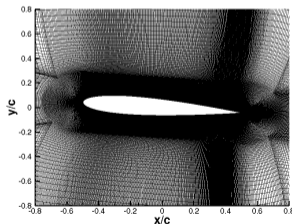
NACA0015: $\alpha = 5^\circ$

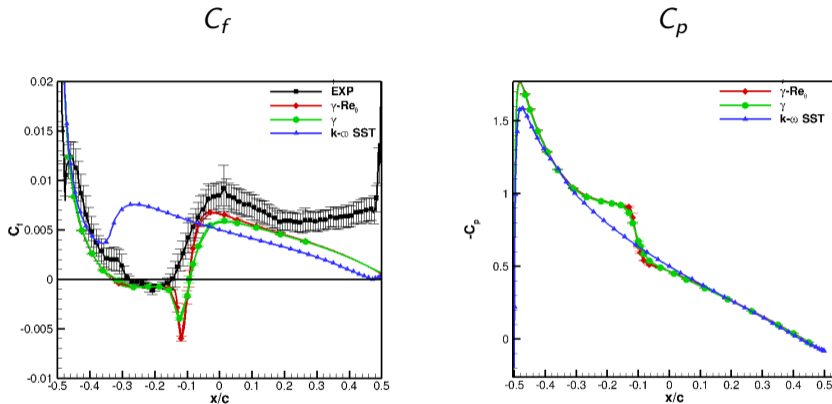
Computational Domain $\alpha = 5^\circ$

Grid	N_{cells}	$N_{\text{cells-foil}}$	y_{max}^+
5	880128	1536	0.375332
6	611200	1280	0.450645
7	391168	1024	0.564111
8	299488	896	0.645391
9	220032	768	0.754048



Meshes provided by IST Lisbon.
Combination of C and O topology to prevent the propagation of very thin cells from the boundary layer through the wake, that would be observed using C-grid topology. Cells with high aspect ratio in the wake strongly penalize the iterative convergence.

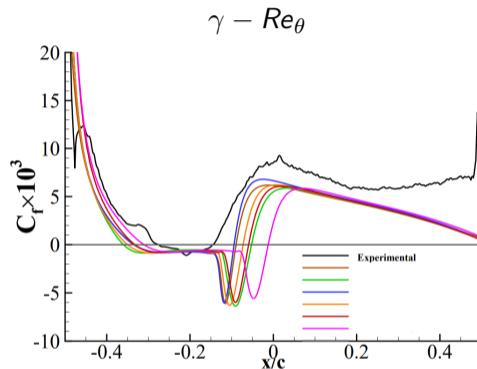
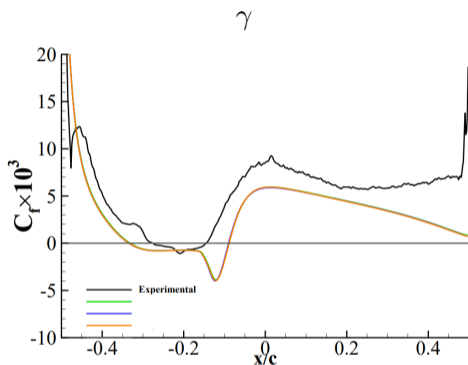


C_f and C_p 

Experiments by Miozzi *et al.* at the CEIMM cavitation tunnel

TSP (Temperature Sensitive Paint): skin friction derived from temporal evolution of the temperature at the surface. Standard deviation of the average in the spanwise direction as experimental uncertainty.

Comparison with other CFD solvers.

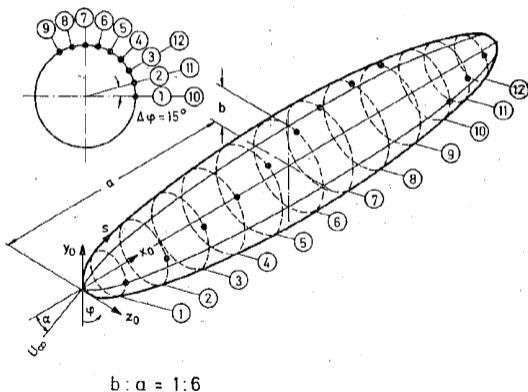


γ implementation is more robust among CFD solvers! However, γ is very sensitive to the mesh refinement.

6:1 Prolate Spheroid

Experimental Campaign at DLR

Measurements performed by Kreplin, [21], in 1985, were conducted in the $3m \times 3m$ low speed wind tunnel at DLR Gottingen.



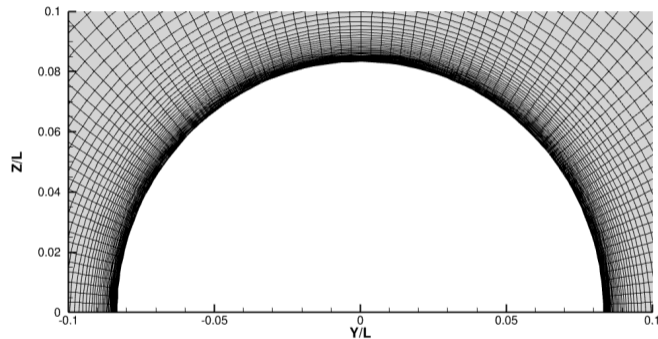
Re	$Tu_{in}(\%)$	$\nu_{t_{in}}/\nu$	$Tu(\%)$
6.5×10^6	0.5	250	0.15

Initial Conditions.
 $Tu \sim 0.1\% - 0.3\%$ reported in the experiments.

Computational Domain

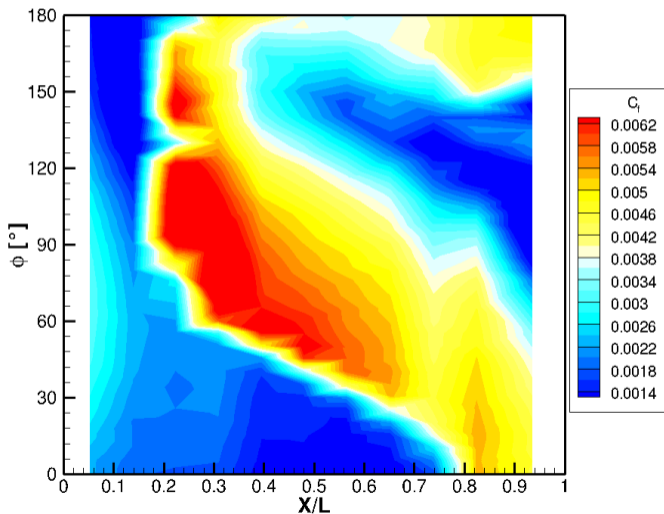
	N_{cells}	$N_{surface}$	y_{max}^+
Grid1	42.6M	126016	0.4
Grid2	28.3M	95816	0.46
Grid3	17.9M	70884	0.54
Grid4	10.3M	48750	0.65
Grid5	5.3M	31504	0.8

Meshes by IST Lisbon.



$X/L = 0$

$$\alpha = 15^\circ$$

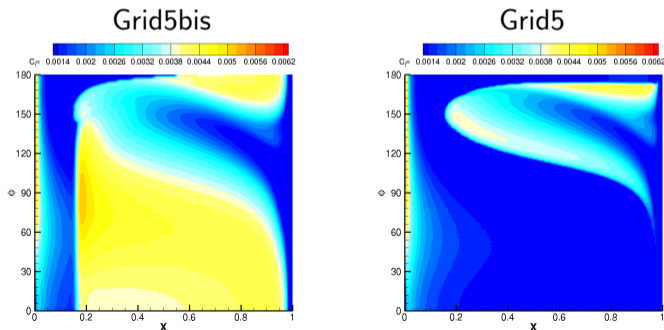
C_f Experimental Results by Kreplin at DLR

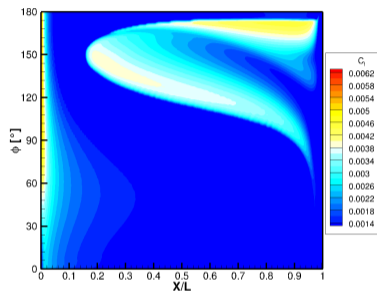
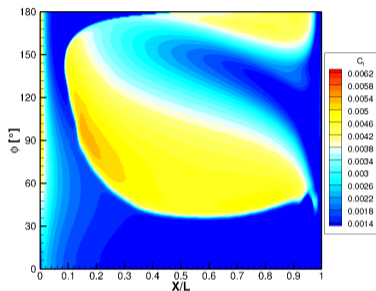
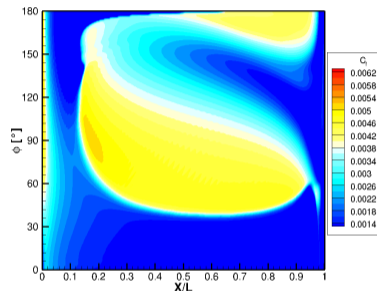
- $\phi = 0^\circ$: windward symmetry plane;
- $\phi = 180^\circ$: leeward symmetry plane;
- Crossflow main transition mechanism at the middle/windward side;
- Streamwise transition close to the symmetry plane.

γ Mesh Dependence: Results w/o Crossflow

	N_{cells}	$N_{surface}$	y_{max}^+	N_{ϕ}	N_x
Grid5bis	4.7M	26048	0.8	~ 138	~ 210
Grid5	5.3M	31504	0.8	~ 88	~ 380

Table: N_x is measured along the upper side of the surface and N_{ϕ} is measured along the plane located at half of the longitudinal length of the surface.



C_f Numerical Results γ w/o crossflow γ +Recalibrated Tc1 $\gamma - Re_\theta + He$

The γ with the new Tc1 performs similarly to $\gamma - Re_\theta + He$.
Both do not predict transition at the windward symmetry plane.

Missing Physical Mechanisms

- Missing physical mechanisms: attachment line instability, interaction T-S waves and CF.

Missing Physical Mechanisms

- Missing physical mechanisms: attachment line instability, interaction T-S waves and CF.
- Contrary to LCTM models, e^N method perform very accurately (Results obtained by DLR). They account for the modes interaction

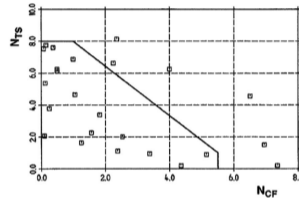
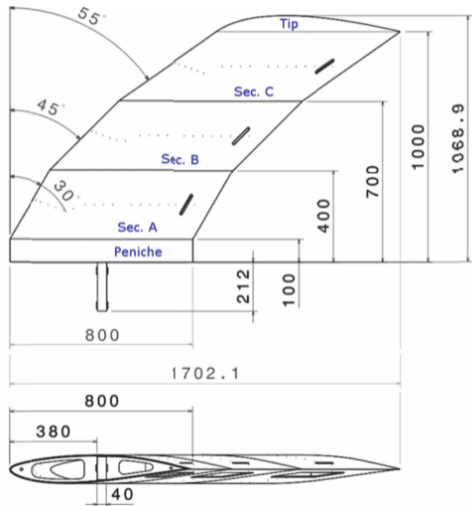


Figure: N_{TS} and N_{CF} stability diagram for the 6:1 prolate spheroid. Figure is reproduced from Stock, [22].

They analyze the instabilities amplification along the physical direction.

As explained in Arnal, 1987, [23], Re_θ is not always a relevant indicator in complicated 3D geometries as the implicit relation exists between Re and the streamwise direction fails.

Sickle Wing

Experiments from Kruse *et al.* and Petzold *et al.* (Different Wind Tunnel DNW-NWB and MUB)

Crossflow modes are highly amplified by the large spanwise gradients created in correspondence of the sweep kinks of the sickle shaped planform and move the transition front upward.

Re	α	$Tu_{in}(\%)$	$\nu_{t_{in}}/\nu$	$Tu(\%)$
2.75×10^6	-2.6°	0.20	2.24	0.17

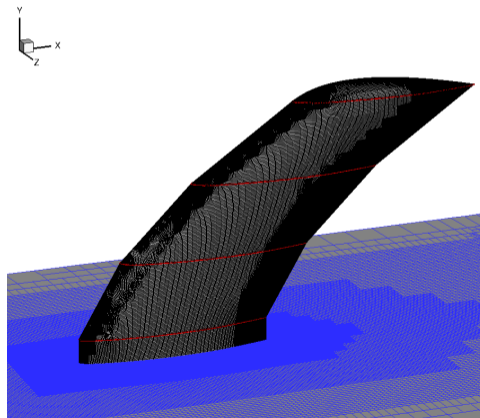
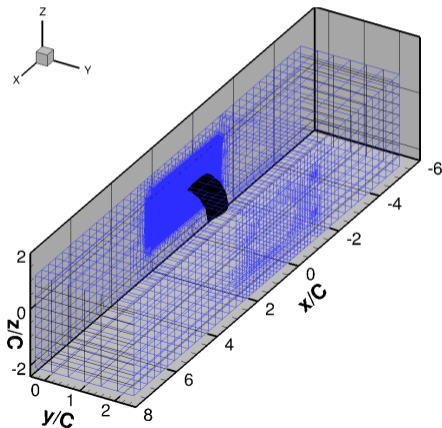
Initial Conditions.

$Tu \sim 0.17\%$ in the experiments from Petzold *et al.*

Sketch of the specimen from Kruse *et al.*(2018).

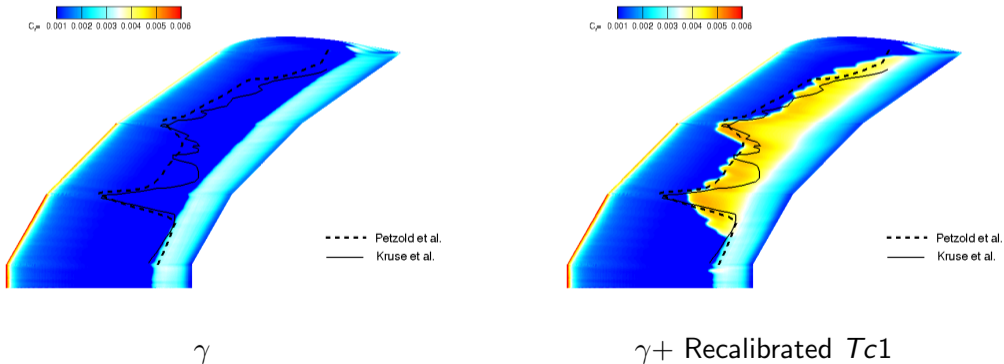
Computational Domain: Unstructured Mesh by Hexpress + Systematic Grid Refinement(SGR)

N_{cells}	$N_{surface}$	y_{max}^+
54M	462243	0.436709



C_f Numerical Results: Upper Surface

- Transition at the bottom is dominated by T-S waves, as suggested by the measured straight transition line.
- Moving upstream in the spanwise direction, the transition process is CF-dominated. The turbulent wedges in the regions of sweep changeover, are related to the strong spanwise gradients.



Contents

- 1 Introduction to Transition Mechanisms
- 2 CFD Transition Modeling
- 3 Numerical Results
- 4 Conclusions and Perspectives

Conclusions I

- Local Correlation Transition Models perform fairly well, but only if we are interested in statistical properties!

Conclusions I

- Local Correlation Transition Models perform fairly well, but only if we are interested in statistical properties!
- They both predict flow features neglected by turbulence models;

Conclusions I

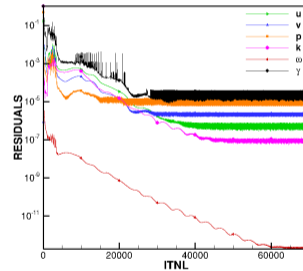
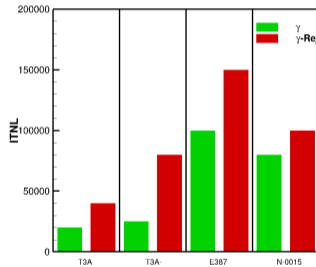
- Local Correlation Transition Models perform fairly well, but only if we are interested in statistical properties!
- They both predict flow features neglected by turbulence models;
- Overall, the two models perform very similarly, critical points (transition start, end, separation, reattachment...) of the transition process are well predicted;

Conclusions I

- Local Correlation Transition Models perform fairly well, but only if we are interested in statistical properties!
- They both predict flow features neglected by turbulence models;
- Overall, the two models perform very similarly, critical points (transition start, end, separation, reattachment...) of the transition process are well predicted;
- γ converges faster than $\gamma - Re_\theta$ and its formulation is more robust (among different solver implementation)! Nevertheless, γ model has to be used with care, because of its mesh dependence (fine grids are needed in both normal and longitudinal directions).

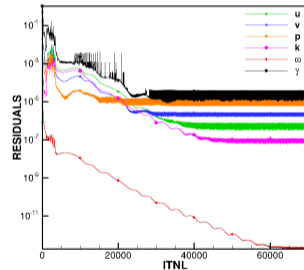
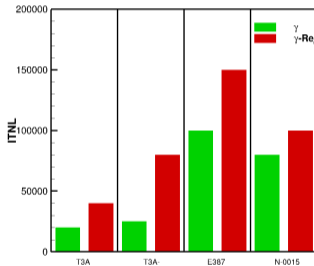
Conclusions II

- Very high computational cost: not smooth functions (min, max operators), laminar flow convergence on grids for turbulent flows.



Conclusions II

- Very high computational cost: not smooth functions (min, max operators), laminar flow convergence on grids for turbulent flows.



- Galilean invariance is an issue for complicated test cases.

What is the future of local correlation transition models? I

The LCTM work fairly good, but they need improvement if we really want to use them as predictive tools!

What is the future of local correlation transition models? II





- The inclusion of new transition mechanisms in the models formulation requires new experimental characterization of the physics.

What is the future of local correlation transition models? II

- The inclusion of new transition mechanisms in the models formulation requires new experimental characterization of the physics.
- What we need from an experimental campaign:
 - Flow pattern at the surface, using sublimating chemicals, such as naphthalene based flow visualization;
 - Perform experiments at different levels of free-stream turbulence intensity by selective removal/addition of turbulence screens;
 - Models with front half with different levels of surface finish to evaluate surface roughness effect ;
 - Use of additional surface-based instrumentation, as microphones, to provide unsteady measurements that would give additional information about the frequency content.
 - More detailed information on the free-stream conditions ought to be given. The turbulence intensity at a given location is not a sufficient information to characterize the turbulence environment and free-decay.

Thank you for your attention!





References I

-  O. Reynolds, “An experimental investigation of the circumstances which determine whether the motion of water shall be direct or sinuous, and of the law of resistance in parallel channels,” *Philosophical Transactions of the Royal society of London*, no. 174, pp. 935–982, 1883.
-  H. Schlichting, *Boundary layer theory*, vol. 960. Springer, 1960.
-  S. Chandrasekhar, *Hydrodynamic and hydromagnetic stability*. Courier Corporation, 2013.
-  P. Drazin and W. Reid, “Hydrodynamic stability,” *Press, Cambridge*, pp. 8–14, 1981.




References II

-  F. Charru, *Hydrodynamic instabilities*, vol. 37. Cambridge University Press, 2011.
-  P. Schmid and D. Henningson, *Stability and Transition in Shear Flows*, vol. 142. Springer Science & Business Media, 2012.
-  N. Shahriari, *On stability and receptivity of boundary-layer flows*. PhD thesis, KTH Royal Institute of Technology, 2016.
-  F. White and I. Corfield, *Viscous fluid flow*, vol. 3. McGraw-Hill New York, 2006.
-  D. Yiming, G. Zhengong, W. Chao, and Q. Huang, “Boundary-layer transition of advanced fighter wings at high-speed cruise conditions,” *Chinese Journal of Aeronautics*, vol. 32, no. 4, pp. 799–814, 2019.





References III

-  D. Poll, “Transition in the infinite swept attachment line boundary layer,” *Aeronautical Quarterly*, vol. 30, no. 4, pp. 607–629, 1979.
-  P. Hall and M. R. Malik, “On the instability of a three-dimensional attachment-line boundary layer: weakly nonlinear theory and a numerical approach,” *Journal of Fluid Mechanics*, vol. 163, pp. 257–282, 1986.
-  P. Spalart, “Direct numerical study of leading-edge contamination,” *Fluid dynamics of three-dimensional turbulent shear flows and transition*, pp. 5–1, 1989.
-  E. H. Hirschel, J. Cousteix, and W. Kordulla, *Three-dimensional attached viscous flow*.
Springer, 2014.




References IV

-  M. O'Meara and T. J. Mueller, "Laminar separation bubble characteristics on an airfoil at low Reynolds numbers," *AIAA Journal*, vol. 25, no. 8, pp. 1033–1041, 1987.
-  D. Lee, S. Kawai, T. Nonomura, M. Anyoji, H. Aono, A. Oyama, K. Asai, and K. Fujii, "Mechanisms of surface pressure distribution within a laminar separation bubble at different Reynolds numbers," *Physics of Fluids*, vol. 27, no. 2, p. 023602, 2015.
-  M. Matsubara and P. H. Alfredsson, "Disturbance growth in boundary layers subjected to free-stream turbulence," *Journal of Fluid Mechanics*, vol. 430, pp. 149–168, 2001.

References V

-  R. S. Rogallo and P. Moin, “Numerical simulation of turbulent flows,” *Annual Review of Fluid Mechanics*, vol. 16, no. 1, pp. 99–137, 1984.
-  H. Choi and P. Moin, “Grid-point requirements for large eddy simulation: Chapman’s estimates revisited,” *Physics of Fluids*, vol. 24, no. 1, p. 011702, 2012.
-  A. Smith and N. Gamberoni, “Transition, pressure gradient, and stability theory. Rep. No. ES 26388, Douglas Aircraft Company,” 1956.
-  M. Högberg and D. Hennigson, “Secondary instability of cross-flow vortices in Falkner–Skan–Cooke boundary layers,” *Journal of Fluid Mechanics*, vol. 368, p. 339–357, 1998.

References VI

-  H. Kreplin, H. Vollmers, and H. Meier, “Wall shear stress measurements on an inclined prolate spheroid in the DFVLR $3m \times 3m$ low speed wind tunnel,” *Data Report, DFVLR IB*, pp. 222–84, 1985.
-  H. W. Stock, “ e^N transition prediction in three-dimensional boundary layers on inclined prolate spheroids,” *AIAA Journal*, vol. 44, no. 1, pp. 108–118, 2006.
-  D. Arnal, “Three-dimensional boundary layer: laminar-turbulent transition,” *Computation of Three-Dimensional Boundary Layers Including Separation*, no. 741, pp. 4–1 – 4–34, 1987.